Optically Unraveling the Edge Chirality-Dependent Band Structure and Plasmon Damping in Graphene Edges

Jiahua Duan, Runkun Chen, Yuan Cheng, Tianzhong Yang, Feng Zhai, Qing Dai, and Jianing Chen**

The nontrivial topological origin and pseudospinorial character of electron wavefunctions make edge states possess unusual electronic properties. Twenty years ago, the tight-binding model calculation predicted that zigzag termination of 2D sheets of carbon atoms have peculiar edge states, which show potential application in spintronics and modern information technologies. Although scanning probe microscopy is employed to capture this phenomenon, the experimental demonstration of its optical response remains challenging. Here, the propagating graphene plasmon provides an edge-selective polaritonic probe to directly detect and control the electronic edge state at ambient condition. Compared with armchair, the edge-band structure in the bandgap gives rise to additional optical absorption and strongly absorbed rim at zigzag edge. Furthermore, the optical conductivity is reconstructed and the anisotropic plasmon damping in graphene systems is revealed. The reported approach paves the way for detecting edge-specific phenomena in other van der Waals materials and topological insulators.

Due to the nontrivial topological structure and unusual quantum confinement, edge plays a critical role in manipulating electrons in Dirac materials[1–4] and constitutes 1D electronic systems with unique properties.[5,6] Graphene, one emerging quantum material, terminates with two types of crystallographic edge orientations (zigzag or armchair) and possesses edge-specific electronic and magnetic properties.[3,7–9] It is theoretically predicted that only zigzag-specific topological structures allow peculiar localized edge state and corresponding quantum properties.[10,11] A variety of first-principle calculations[12–14] also predict that the zigzag edge provides a natural vehicle to realize 1D confinement of electrons and topologically protected state, which is very important for nanoscale information transduction and spintronics. Experimentally, the enhanced DC (direct current) conductance and the super-currents involved electronic guided-wave states related to zigzag chirality have become a governing factor in graphene devices (GDs) and provided a novel transmission mode of electronic stream.[15,16] However, it is challenging to distinguish the edge-specific phenomena from bulk response. The optical properties of graphene electronic edge states and its real-space imaging still remain ambiguous due to the limited spatial resolution in standard far-field methods. The tunability of edge states, prerequisite for future nano-optoelectronic devices, is not accomplished, either.

Here, we report the first observation of enhanced near-field optical response localized at zigzag and bilayer edges, revealing edge-specific electronic band structure. The width of strongly absorbed rim at zigzag edge can be tuned from 59 to 37 nm by changing the imaging wavelength in the infrared region. By numerical simulation, we reconstruct the spatial distribution of optical conductivity at different edges, and we attribute the enhanced optical conductivity to the edge-band for zigzag and charge accumulation for armchair, respectively. Furthermore, the anisotropic plasmon damping is explored, which is important for the future graphene plasmonic devices. The experimental approach shows great potential for studying optical response of edge-specific phenomena and other topological properties in van der Waals materials.

Different from armchair-terminated carbon networks, the zigzag-termination shows a large density of states at Dirac point (called as edge-band, as shown in **Figure 1**a), which bends toward the Fermi level.[12–16] As a result of its quantum channeling effect, the bilayer edge exhibits similar sophisticated mini-bands[17] as zigzag. Recently, the observation of edge plasmons in graphene nanoribbon[18–21] and superlattice plasmons in graphene-hBN moiré structures[22] opens doors for exploring topological properties and electronic structure via polaritonic probes. It is thus feasible to reconstruct optical

Dr. J. Duan, R. Chen, Prof. Y. Cheng, Prof. T. Yang, Prof. J. Chen
Institute of Physics
Chinese Academy of Sciences
100190 Beijing, China
E-mail: jnchen@iphy.ac.cn
Dr. J. Duan, R. Chen, Prof. Y. Cheng, Prof. T. Yang, Prof. J. Chen
School of Physical Sciences
University of Chinese Academy of Sciences
100049 Beijing, China
Prof. F. Zhai
Department of Physics
Zhejiang Normal University
321004 Jinhua, China
Prof. Q. Dai
National Center for Nanoscience and Technology
100190 Beijing, China
E-mail: daiq@nanoctr.cn
Prof. J. Chen
Collaborative Innovation Center of Quantum Matter
100190 Beijing, China

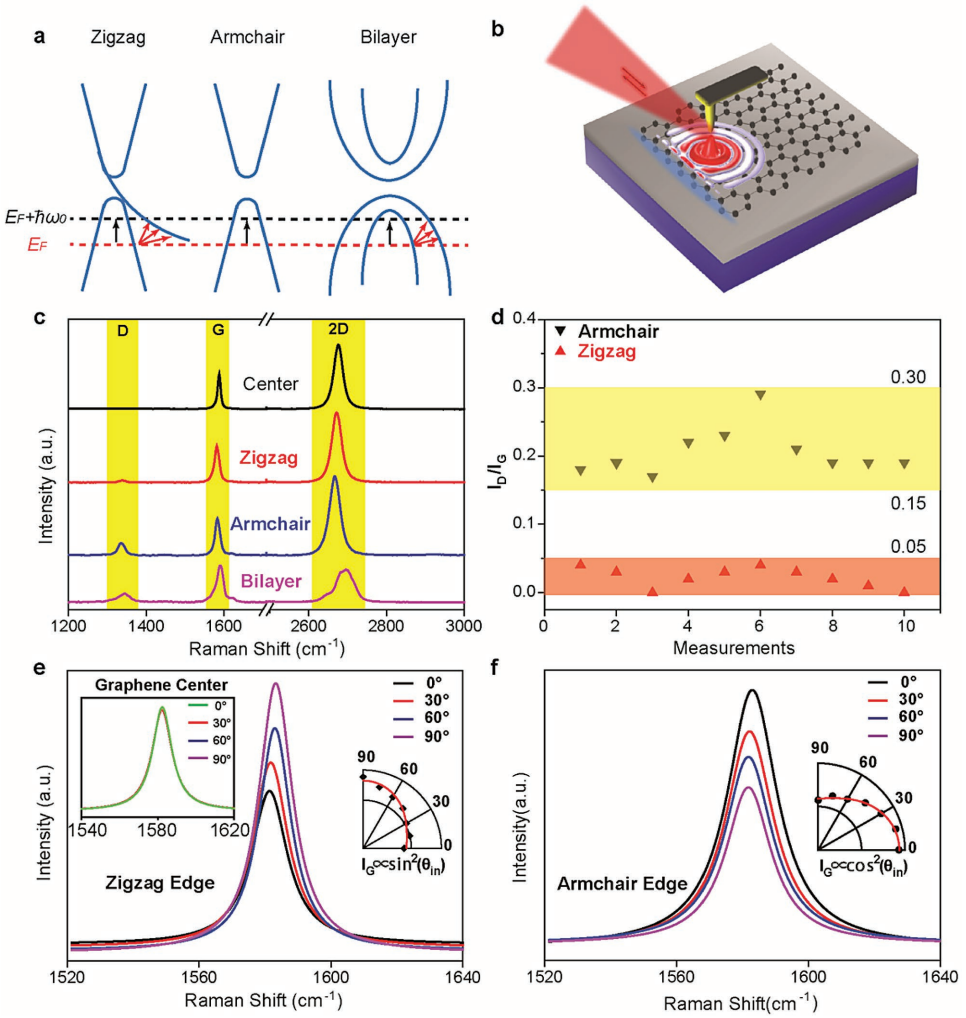

Figure 1. Edge chirality determination through Raman spectroscopy. a) The electronic structure of zigzag, armchair, and bilayer edge in pristine graphene sample. The red arrows indicate additional optical absorption channel due to the edge-band structure at zigzag and sub-bands at bilayer edge. b) Diagram of the experimental apparatus used to launch propagating plasmon waves in graphene. The plasmon waves serve as a polaritonic probe to detect localized electronic edge state. c) Typical Raman spectra of graphene center, zigzag, armchair, and bilayer edge, respectively. We normalize the Raman spectra with the intensity of G mode. Compared with zigzag edge, the armchair one shows stronger $I(D)$, which is important for the determination of edge chirality. The Bernal-stacking bilayer edge can be identified by its distinctive Raman response, which shows wider (≈54 cm^{-1}) and four-Lorentzian-component shape 2D peak. d) The statistic for $I(D)/I(G)$, which stays homogenous at the entire graphene edge (armchair shows larger ratio than zigzag). e,f) Polarized Raman spectra of zigzag and armchair edge, showing different polarization dependence of the G mode. Inset: polar plots of the integrated intensity of the G mode at zigzag ($I_G \propto \sin^2(\theta_{in})$) and armchair ($I_G \propto \cos^2(\theta_{in})$) edge, respectively. The θ_{in} represents angle between incident polarization and graphene edges. The Raman spectra taken from the graphene center show polarization independence (inset in e).

complex conductivity ($\sigma(\omega) = \sigma_1(\omega) + i\sigma_2(\omega)$) from polaritonic images, containing information of both electronic and lattice dynamics.[23] Given the fact that the complex conductivity determines the plasmonic reflections at graphene edge, the plasmon polariton wave provides an unprecedented edge-selective probe. The propagating graphene plasmons are launched and detected simultaneously using scattering-type scanning near-field optical microscopy (s-SNOM, schematic in Figure 1b). The metallic tip acts as an antenna to generate strongly enhanced electric field and compensate the momentum mismatch. We normalized near-field amplitude $s_4(\omega) = s_4^0(\omega)/s_4^{si}(\omega)$. Here, $s_4^0(\omega)$ and $s_4^{si}(\omega)$ are the fourth-order demodulated harmonics of the near-field amplitude detected for graphene and Si standard reference sample, respectively. We extract the wavelength of plasmon wave (λ_p) due to the formation of fringes with a period of $\lambda_p/2$ coming from the interference between tip-launching and edge-reflecting plasmon.[24,25] The amplitude of overall near-field scattering signal, plasmonic wavelength, and propagation damping give entire information of the complex conductivity of graphene at the incident frequency.

Our monolayer graphene is mechanically exfoliated on 285 nm thick SiO_2/Si substrates, and its properties (including crystalline quality, morphology, doping concentration, and layer thickness) are characterized through optical contrast measurements, atomic force microscopy (AFM), and Raman spectroscopy (see more details in the Supporting Information). We

choose freshly fabricated graphene with clean edges for the near-field optical measurements in order to avoid the contamination at ambient atmosphere. In Figure 1c (black solid line), the single Lorentz fitting of 2D peak (≈2700 cm^{-1}), narrow bandwidth of both G and 2D peak (≈25 cm^{-1}), absence of D peak (≈1350 cm^{-1}), and the ratio (≈2) between 2D and G peak are the distinct characteristics of our monolayer graphene with high quality. The line-scan Raman mapping determines the accurate position of edge (Figure S3, Supporting Information). Figure 1c also shows the typical Raman spectra collected at zigzag (red), armchair (blue), and bilayer edges (pink), respectively. The spectra are normalized with G mode, which is independent of edge type. The armchair edge scatters electrons from one to another valley near the Dirac points (K to K' intervalley scattering), but zigzag do not.[26,27] Therefore, the double resonance Raman process can only be activated at armchair structure (stronger D band), while same process is forbidden for a zigzag edge (weaker or vanished D band). Compared with folding double-layer edge (similarly sharp and symmetric single Lorentzian component 2D peak), the Bernal-stacking bilayer edge can be identified by its distinctive Raman response, which shows wider (≈54 cm^{-1}) and four-Lorentzian-component shape 2D peak.[28] In order to guarantee the genuineness of edge chirality, we make statistics for the I_D/I_G intensity ratio by conducting ten Raman measurements of each edge at different positions. The I_D/I_G ratio stays in the range of (0.15, 0.3) at armchair and (0, 0.05) at zigzag edge (Figure 1d). Furthermore, we carry out the polarization-dependent Raman characterization at armchair and zigzag edges. The two degenerate components of the graphene G mode (LO phonon at armchair and TO phonon at zigzag) cause the opposite polarized dependences. In Figure 1e, the I_G reaches minimum value at $\theta = 0°$ and maximum value at $\theta = 90°$ at zigzag edge (fitting with the tendency of $\sin^2(\theta)$, here, θ is the angle between incident polarization and graphene edge), which is opposite to the armchair one (fitting with the tendency of $\cos^2(\theta)$).[29] This polarized dependence only occurs at 1D edge and disappears in graphene center (inset in Figure 1e). All the Raman measurements show clear evidences to distinguish the three types of graphene edge, which are the fundamentals for the study of edge state.

In **Figure 2**, we show optical nanoimaging of different edge structures and plasmonic wavelength dependence on Fermi level and incident frequency. The near-field optical images of zigzag (Figure 2b), armchair (Figure 2f), and bilayer edge (Figure 2j) are collected at IR frequency ω_0 = 930 cm^{-1}. The AFM topography maps (Figure 2a,e,i) show smooth graphene surface free of wrinkles or defects. The corresponding line profiles (Figure 2c,g,k) indicate that the heights of monolayer and bilayer graphene are ≈0.5 and ≈0.9 nm, respectively. The fringes parallel to the edge direction appear in the near-field

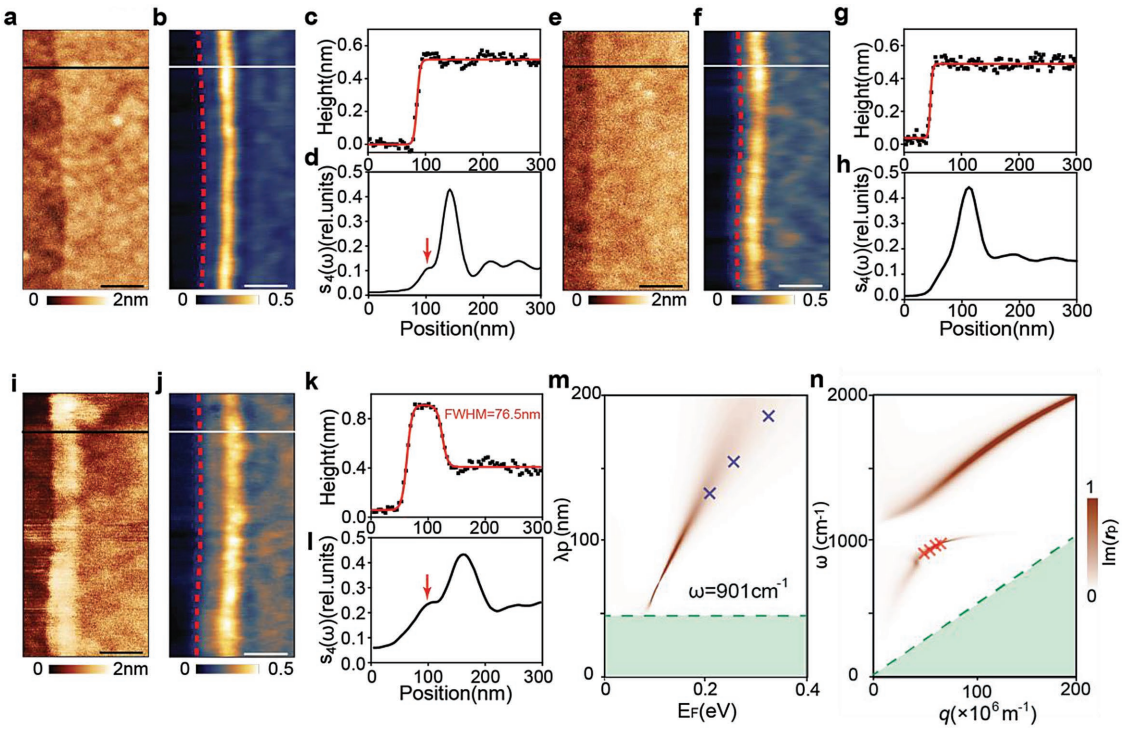

Figure 2. Infrared nanoimaging of zigzag, armchair, and bilayer edge. a,e,i) AFM images of zigzag, armchair, and bilayer edge structure. The darker area corresponds to the SiO_2/Si substrate. c,g,k) AFM line profiles obtained from the black solid line in (a), (e), and (i), respectively. b,f,j) Nano-infrared images of zigzag, armchair, and bilayer edge, respectively. In the optical image of zigzag (b) and bilayer edge (j), there is an obvious bright stripe between the graphene edges (marked by red dashed lines) and dominated plasmonic fringe, which is ignorable in armchair (f). The incident frequency is 930 cm^{-1}. d,h,l) Plasmonic line profiles from the white solid line in (b), (f), and (j), respectively. The shoulder-like peak is observed in zigzag (d) and bilayer edge (l). Oppositely, the plasmonic line profile from armchair (h) shows no shoulder-like peak. Scale bar, 100 nm. m,n) Plasmon wavelength dependence on Fermi level (ω_0 = 901 cm^{-1}) and incident frequency (E_F = 0.22 eV). Crosses show the extracted experimental values and the background color shows the imaginary part of the Fresnel reflection coefficient. The electronic intraband Landau damping region is shaded green.

images, which are similar to several recent studies.[22,24,25] Compared with Figure 2f (armchair), the image in Figure 2b (zigzag) and Figure 2j (bilayer) show a strip of enhanced near-field amplitude at the edge area before the first plasmon fringe. The line profiles of near-field amplitude are plotted in Figure 2d,h,l for zigzag, armchair, and bilayer edge, respectively. Besides the common fringes decaying away from the edge, there is a shoulder-like peak located at the zigzag edge (red arrow in Figure 2d). However, this shoulder peak is negligible at armchair edges (Figure 2h). Compared with zigzag or armchair structure, AFM measurement can precisely identify the width of bilayer edge (full width half maximum (FWHM) ≈ 76.5 nm), and there is shoulder-like peak at bilayer edge (Figure 2l) as well. 1D edge plasmon[20,21] is not observed here, indicating that there are no reflectors (sharp corners or small defects) in our smooth edge structures, which are good for the near-field imaging. Figure S12 (Supporting Information) shows that the edge plasmon appears if the measurement is done at the edges with sharp corner or small defects. In Figure 2m,n, we show detailed study of the plasmonic wavelength dependence on Fermi level and incident frequency, together with the calculated imaginary part of the Fresnel reflection coefficient (background color). Although the graphene samples are not gate-tunable in this work, we record the effect of carrier density variation through measuring a large number of samples with different natural doping. At fixed imaging frequency, the longer wavelength (λ_p) corresponds to higher Fermi level,[30] in accordance with the scaling relation between λ_p and Fermi level as Equation (1)

$$\lambda_p(\omega) = \frac{8\pi e^2 E_F}{\hbar^2 \omega^2 [1+\varepsilon_{sub}(\omega)]} \quad (1)$$

The experimentally extracted wavelengths (isolated crosses in Figure 2m,n) show good agreement with the theoretical calculation, indicating successful nanoimaging of graphene plasmons.

In order to quantify width of the shoulder-like peak, we define effective width (W_{eff}) in the infrared nanoimages as abrupt changing region of curvature of plasmonic line profiles at edge area, which is calculated through the first-order differential method. An obvious peak appears in the derivative signals (zigzag in **Figure 3**a and bilayer in Figure 3b). We plot the W_{eff} (or can be regarded as the interaction region between edge state and graphene plasmon) in Figure 3c with different Fermi levels and different incident frequencies. It is worth noting that the effective width probed in nanoimages does not represent the actual width of optical edge features. This is because that the extracted W_{eff} contains the edge–plasmon interaction and broadening effect from AFM tip,[10] whose typical curvature is about 25 nm. When we remove the tip broadening effect by dividing the size of tip apex,[15] we come to the scale of optical feature of zigzag edge as about 2–3 nm, correlating with the tight-binding model calculation which predicts edge states with width of ≈2 nm at zigzag termination of graphene.[10–13] For the

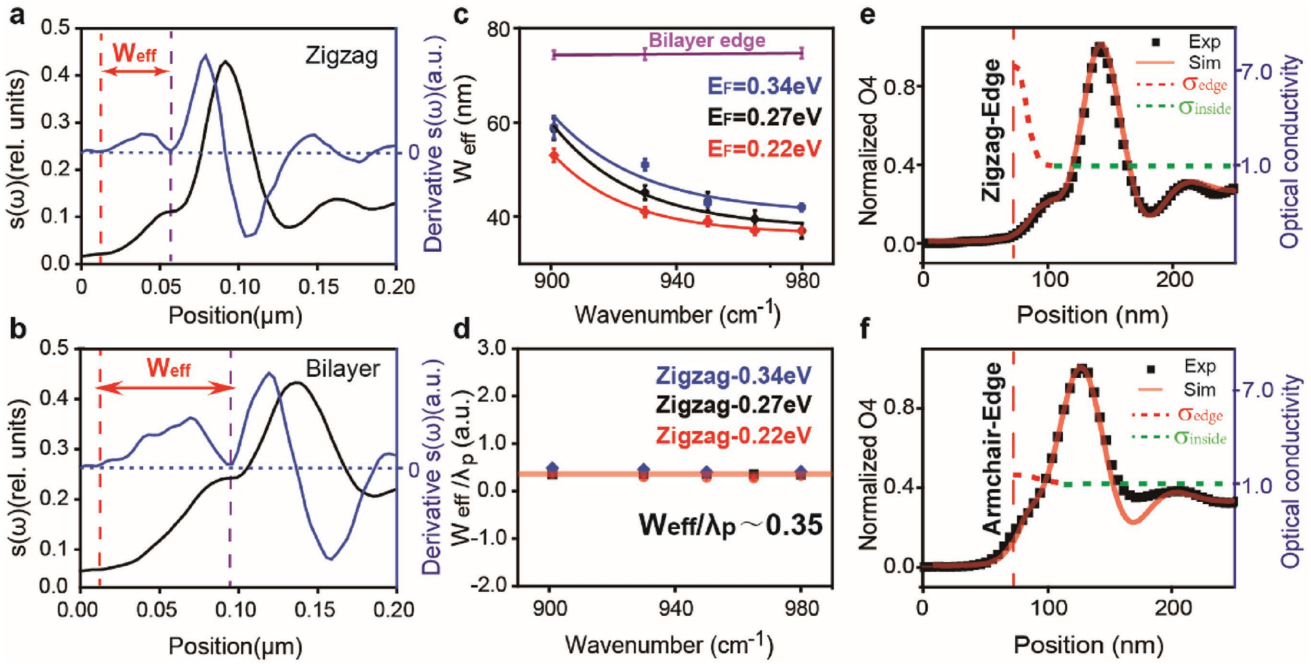

Figure 3. Reconstruct the optical conductivity and control optical features of graphene edge. a,b) The first derivation operation of the optical amplitude is conducted to extract the effective width of shoulder-like peak. The change of original curve (black line) slope caused by shoulder-like peak induces an obvious peak in the derivative amplitude curve (blue line). The effective width (W_{eff}) is directly extracted through this mathematical calculation, as shown in (a) (zigzag) and (b) (bilayer edge). c) Experimentally extracted W_{eff} as a function of incident frequency and Fermi level. Due to the strong localized effect from bilayer structure, the independence of incident frequency is observed at the bilayer edge. d) Experimentally obtained intrinsic property of graphene edge state ($W_{eff}/\lambda_p \approx 0.35$), which shows independent of incident frequency and Fermi level. e) The optical conductivity is extracted from the fitting of plasmonic line profile at zigzag edge. The black squares are the experimental data; the red solid line is the theoretical fitting using the dipole model. The enhancement of $\sigma(\omega)$ caused by edge state is shown as dashed line. f) The numerical simulation of plasmonic line profile at armchair edge.

case of bilayer graphene edge (Figure 3c), the extracted W_{eff} of bilayer edge (≈74.5 nm) is approximately equal to the FWHM of its morphological structure (≈76.5 nm) no matter what the incident frequency is. This similarity further confirms that the strongly absorbed rim at edge area is caused by sophisticated sub-band electronic structures. When the influence of plasmon dispersion at zigzag edge is removed by dividing W_{eff} with plasmonic wavelength (λ_p), we find the ratio of these two quantities remains as a constant of $W_{eff}/\lambda_p \approx 0.35$, indicating that the appearing bright rim is an intrinsic property of zigzag edge, which does not rely on measurement conditions (Figure 3d). We measured several zigzag edges with different Fermi levels and W_{eff}/λ_p stays at 0.35 ± 0.08. When we measure samples with higher Fermi level or increase incident wavelength, the W_{eff} shows an increasing tendency (Figure 3c), which is explained by Equation (1).

In order to get more insights of the optical features at different graphene edges, we perform numerical simulations of plasmon reflections at zigzag and armchair by a dipolar tip model as shown in Figure 3e,f (details in the Experimental Section and the Supporting Information). The black squares are the experimental data and the red solid lines are the theoretical fitting. In the simulation, we separate optical conductivity of graphene into two sections: edge conductivity (σ_{edge}, red dashed lines) and bulk conductivity (σ_{inside}, green dashed lines). The σ_{inside} is calculated from experimental measurements, including Raman spectrum (Figure S5, Supporting Information) and near-field images (Figure 2), based on Drude model. In order to get best fit of plasmonic profiles, we need to choose different edge conductivity profiles at zigzag and armchair, respectively. Regardless of the edge chirality, the edge conductivity is larger than the conductivity inside graphene. However, the enhancements factor ($\sigma_{edge}/\sigma_{inside}$) is different for zigzag (≈7.2) and armchair (≈1.6). The slightly increased σ_{edge} at armchair can be attributed to charge accumulation near edge, which is confirmed by Raman spectra ($E_{F\text{-}edge}/E_{F\text{-}inside} \approx 1.4$ in Figure S5, Supporting Information). Compared with armchair edges, the strongly enhanced conductivity at zigzag indicates that there are more factors leading to this extraordinary optical absorption other than charge accumulation. This additional absorption in near-field images thus can be attributed to the additional optical transition caused by the edge-band structure at zigzag edges.[22] At the same time, it should be noted that the extracted changing region of σ_{edge} is on the same order of the effective width (≈50 nm), due to the similar broadening effect observed at graphene grain boundary.[31] To the best of our knowledge, this is the first time to distinguish the enhanced optical conductivity caused by sub-band structure from the enhanced conductance along edges due to the charge accumulation.

Previous nano-infrared images of graphene plasmon[24,25] ignore the influence from the edge chirality. In fact, the edge possesses ability in selecting specific momentums of excited electrons (inset of **Figure 4**a,b, Supporting Information). It is reasonable to expect that the electronic edge state at zigzag edge would influence the scattering behavior of plasmon, compared with armchair. Thus, the edge chirality needs to be taken into

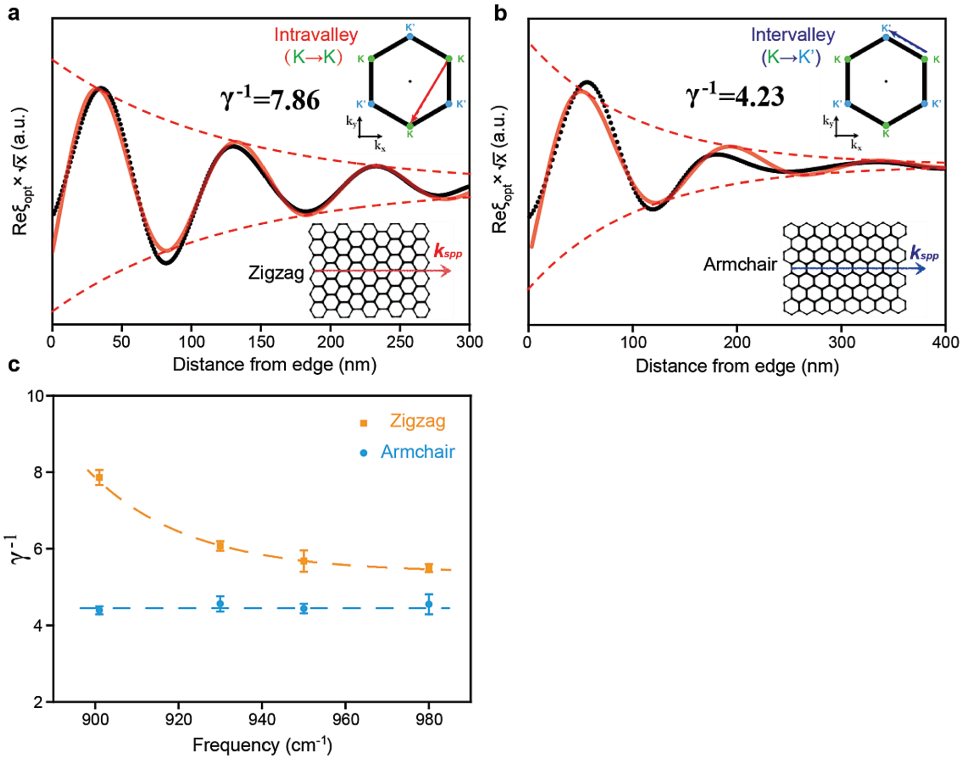

Figure 4. The different plasmon damping at zigzag and armchair edge caused by edge state and defect scattering. a,b) Extraction of plasmon damping at zigzag and armchair edge, respectively. Black dots show the experimental near-field signal, which are averaged along the edge and with a subtraction of background through FFT. The detailed method is described in the Supporting Information. The inset shows the intravalley and intervalley scattering process at zigzag and armchair. c) Inverse damping rate as a function of incident frequency at zigzag and armchair edge.

account when we study the damping rate of graphene plasmon. The decaying propagation of graphene plasmons[30] can be described by Equation (2)

$$\xi_{opt} = A\frac{e^{i2qx}}{\sqrt{x}} + B\frac{e^{iqx}}{x} \quad (2)$$

here, ξ_{opt} is complex near-field signal. A, B are fitting parameters, q is the plasmonic wavevector. The first term is the tip-launched circular wave, which propagates radially outward from the tip and reflects back upon reaching graphene edge with a travelling distance of $2x$. The second term is the edge-launched plane wave with a travelling distance of x, which is strongly weaker compared with tip-launching plasmon. Because the $e(i2qx)$ component dominates in our experiments, we can separate the $e(iqx)$ component with Fourier analysis.[30] In Figure 4a,b, we isolate the damping decay and extract the inverse damping ratio $\gamma_p^{-1} = \mathrm{Re}(q)/\mathrm{Im}(q)$, which differ for zigzag edge $(\gamma_p^{-1} \approx 8)$ and armchair edge $(\gamma_p^{-1} \approx 4)$. The different electronic scattering mechanism at zigzag (intravalley) and armchair (intervalley) induce the influence from edge chirality on the plasmonic damping. Given enhanced optical conductivity at zigzag and stronger D peak at armchair, their dominated factor to determine γ_p^{-1} is electronic edge state and defect scattering, respectively. This explains the relation between γ_p^{-1} and incident frequency, which is monotonic decreasement (similar to W_{eff}) at zigzag and independence at armchair, as shown in Figure 4c. It is observed that the plasmonic propagation damping at zigzag is smaller than armchair at all incident frequencies. Although the protected mechanism stays ambiguous (impacts from many-body interaction are complicated in graphene), the better candidate for future graphene edge plasmonic devices is smoothed zigzag type.

In summary, we show that the plasmon acts as a neat probe to unravel the edge-specific electronic band structure with nanoscale spatial resolution. By near-field imaging of well-prepared graphene edges, the optical response of edge state is revealed. Our experimental results show that near-field optical imaging has high sensitivity on detecting subtle electronic features of a few nanometers at room temperatures, ambient condition, and contact free. We both experimentally and theoretically show the influence from edge chirality on optical conductivity and plasmonic properties in graphene system. We believe this method has great potential for studying edge related phenomena in other plasmonic and photonic system such as carbon nanotubes, boron nitride, and topological insulators.

Experimental Section

Sample Preparation and Characterization: Microcrystals of graphene were mechanically exfoliated from bulk graphite samples and then transferred to 285 nm thick SiO_2/Si substrate. The optical microscopy, AFM, and Raman spectroscopy are used to identify the monolayer graphene without defects. In order to determine the position of graphene edge, we perform 1D Raman mapping with light polarized parallel to the edge direction and define the graphene edge where the maximum I_D is, when I_G and I_{2D} are simultaneously half the inside intensity. The Raman response on edge area identifies the types of edge. Besides, the Fermi level of graphene is extracted from Raman spectra based on theoretical calculations (see more details in the Supporting Information).

Infrared s-SNOM Measurements: The nanoimaging experiments in the main text and the Supporting Information are performed using a s-SNOM. The s-SNOM is a commercial system (Neaspec GmbH) equipped with quantum cascade lasers (QCLs from Daylight Solutions). The incident frequency spans from 901 to 985 cm^{-1}. The s-SNOM is based on an AFM operating in the tapping mode with $\Omega \approx 300$ kHz and an amplitude of ≈30 nm. A pseudo-heterodyne interferometric method was applied to extract both the near-field amplitude and phase of graphene plasmons. The near-field signal is demodulated at a fourth harmonic in order to suppress background signal. Near-field amplitude $s_4(\omega) = s_4^0(\omega)/s_4^{si}(\omega)$ was normalized. Here, $s_4^0(\omega)$ and $s_4^{si}(\omega)$ are the fourth demodulated harmonics of the near-field amplitude detected for graphene and Si standard reference sample, respectively. All nano-IR imaging experiments are conducted at ambient atmosphere.

Dispersion of Graphene Plasmon: In order to obtain dispersion of plasmon polariton, the complex reflectivity $r_p(q,\omega)$ of graphene/substrate structure under a p-polarized incident electromagnetic wave, coupling with graphene plasmon at a finite wavevector was calculated. The Fresnel reflection coefficients (see more details in the Supporting Information) is expressed as[32]

$$r_p = \frac{\varepsilon_2 k_{1z} - \varepsilon_1 k_{2z} + k_{1z}k_{2z}\sigma(q,\omega)/(\varepsilon_0\omega)}{\varepsilon_2 k_{1z} + \varepsilon_1 k_{2z} + k_{1z}k_{2z}\sigma(q,\omega)/(\varepsilon_0\omega)} \quad (3)$$

where ε_1 and ε_2 are the relative permittivity of air and the substrate, respectively, ε_0 is the vacuum permittivity, ω is the angular frequency of the incident plane wave, and q is the wavevector of plasmon. The k_{1z} and k_{2z} represent the z-components of the wavevector of the incident and the transmitted plane waves, respectively. The $\sigma(q,\omega)$ is conductivity of graphene, and derived within the random phase approximation (RPA). Since the wavevector of surface graphene plasmon is related to the reflectivity, the maxima imaginary part of r_p represents a maximum dissipation and gives rise to the dispersion of graphene plasmon.

Numerical Simulations: The numerical calculations are done by the finite boundary elements method, using the commercial software package COMSOL in a Wave Optics Module. The graphene is modeled as an infinite thin conducting layer whose conductivity is given by the Drude mode. The extracted conductivity has different distributions at zigzag and armchair edge. A vertically oriented electric point dipole is set to replace the tip to excite graphene plasmon.[21] A point probe is set to recording the $|E|$ (absolute value of electric field) around 10 nm above graphene when the dipole (30 nm above sample) scanning from SiO_2 substrate to graphene. The dielectric functions for SiO_2 are taken from ref. [33]. More details about numerical simulation are provided in the Supporting Information.

Supporting Information

Supporting Information is available from the Wiley Online Library or from the author.

Acknowledgements

This work was supported by the National Key Research and Development Program of China (2016YFA0203500), National Natural Science Foundation of China (Grant Nos. 11474350 and 11504245), J.C. is supported by the Youth Innovation Promotion Association of CAS.

Conflict of Interest

The authors declare no conflict of interest.

Keywords

chirality, damping, graphene edges, optical conductivity, plasmons

[1] Y. Son, M. L. Cohen, S. G. Louie, *Nature* **2006**, *444*, 347.
[2] N. Tombros, C. Jozsa, M. Popinciuc, H. T. Jonkman, B. J. Van Wees, *Nature* **2007**, *448*, 571.
[3] G. Z. Magda, X. Jin, I. Hagymasi, P. Vancso, Z. Osvath, P. Nemesincze, C. Hwang, L. P. Biro, L. Tapaszto, *Nature* **2014**, *514*, 608.
[4] O. V. Yazyev, M. I. Katsnelson, *Phys. Rev. Lett.* **2008**, *100*, 047209.
[5] L. Liu, J. Park, D. A. Siegel, K. F. Mccarty, K. W. Clark, W. Deng, L. Basile, J. C. Idrobo, A. Li, G. Gu, *Science* **2014**, *343*, 163.
[6] A. F. Young, J. Sanchezyamagishi, B. Hunt, S. H. Choi, K. Watanabe, T. Taniguchi, R. C. Ashoori, P. Jarilloherrero, *Nature* **2013**, *505*, 528.
[7] D. Abajo, F. J. Garcia, *ACS Photonics* **2014**, *1*, 135.
[8] P. A. D. Gonçalves, N. M. Peres, *An Introduction to Graphene Plasmonics*, World Scientific, Singapore **2016**.
[9] J. Rodrigues, P. A. D. Goncalves, N. F. G. Rodrigues, R. M. Ribeiro, J. M. B. L. D. Santos, N. M. R. Peres, *Phys. Rev. B* **2011**, *84*, 155435.
[10] M. Fujita, K. Wakabayashi, K. Nakada, K. Kusakabe, *J. Phys. Soc. Jpn.* **1996**, *65*, 1920.
[11] K. Nakada, M. Fujita, G. Dresselhaus, M. S. Dresselhaus, *Phys. Rev. B* **1996**, *54*, 17954.
[12] W. Yao, S. A. Yang, Q. Niu, *Phys. Rev. Lett.* **2009**, *102*, 096801.
[13] T. Wassmann, A. P. Seitsonen, A. M. Saitta, M. Lazzeri, F. Mauri, *Phys. Rev. Lett.* **2008**, *101*, 096402.
[14] Y. Son, M. L. Cohen, S. G. Louie, *Phys. Rev. Lett.* **2006**, *97*, 216803.
[15] J. Chae, S. Jung, S. Woo, H. Baek, J. Ha, Y. J. Song, Y. Son, N. B. Zhitenev, J. A. Stroscio, Y. Kuk, *Nano Lett.* **2012**, *12*, 1839.
[16] M. T. Allen, O. Shtanko, I. C. Fulga, A. R. Akhmerov, K. Watanabe, T. Taniguchi, P. Jarilloherrero, L. S. Levitov, A. Yacoby, *Nat. Phys.* **2015**, *12*, 128.
[17] Y. Zhang, T. Tang, C. Girit, Z. Hao, M. C. Martin, A. Zettl, M. F. Crommie, Y. R. Shen, F. Wang, *Nature* **2009**, *459*, 820.
[18] P. A. D. Gonçalves, S. Xiao, N. M. R. Peres, N. A. Mortensen, *ACS Photonics* **2017**, *4*, 3045.
[19] S. Thongrattanasiri, A. Manjavacas, F. J. G. De Abajo, *ACS Nano* **2012**, *6*, 1766.
[20] Z. Fei, M. Goldflam, J. Wu, S. Dai, M. Wagner, A. S. Mcleod, M. Liu, K. W. Post, S. Zhu, G. C. A. M. Janssen, *Nano Lett.* **2015**, *15*, 8271.
[21] A. Y. Nikitin, P. Alonsogonzalez, S. Velez, S. Mastel, A. Centeno, A. Pesquera, A. Zurutuza, F. Casanova, L. E. Hueso, F. H. L. Koppens, *Nat. Photonics* **2016**, *10*, 239.
[22] G. Ni, H. Wang, J. Wu, Z. Fei, M. Goldflam, F. Keilmann, B. Ozyilmaz, A. H. C. Neto, X. Xie, M. M. Fogler, *Nat. Mater.* **2015**, *14*, 1217.
[23] D. N. Basov, M. M. Fogler, F. J. G. De Abajo, *Science* **2016**, *354*, 195.
[24] J. Chen, M. Badioli, P. Alonsogonzalez, S. Thongrattanasiri, F. Huth, J. Osmond, M. Spasenovic, A. Centeno, A. Pesquera, P. Godignon, *Nature* **2012**, *487*, 77.
[25] Z. Fei, A. S. Rodin, G. O. Andreev, W. Bao, A. S. Mcleod, M. Wagner, L. M. Zhang, Z. Zhao, M. H. Thiemens, G. Dominguez, *Nature* **2012**, *487*, 82.
[26] L. G. Cancado, M. A. Pimenta, B. R. A. Neves, M. S. S. Dantas, A. Jorio, *Phys. Rev. Lett.* **2004**, *93*, 247401.
[27] B. Krauss, P. Nemesincze, V. Skakalova, L. P. Biro, K. V. Klitzing, J. H. Smet, *Nano Lett.* **2010**, *10*, 4544.
[28] Z. Fei, E. G. Iwinski, G. Ni, L. M. Zhang, W. Bao, A. S. Rodin, Y. S. Lee, M. Wagner, M. Liu, S. Dai, *Nano Lett.* **2015**, *15*, 4973.
[29] C. Cong, T. Yu, H. Wang, *ACS Nano* **2010**, *4*, 3175.
[30] A. Woessner, M. B. Lundeberg, Y. Gao, A. Principi, P. Alonsogonzalez, M. Carrega, K. Watanabe, T. Taniguchi, G. Vignale, M. Polini, *Nat. Mater.* **2014**, *14*, 421.
[31] Z. Fei, A. S. Rodin, W. Gannett, S. Dai, W. Regan, M. Wagner, M. Liu, A. S. Mcleod, G. Dominguez, M. H. Thiemens, *Nat. Nanotechnol.* **2013**, *8*, 821.
[32] O. Keller, *Phys. Today* **2006**, *60*, 62.
[33] Z. Fei, G. O. Andreev, W. Bao, L. M. Zhang, A. S. Mcleod, C. Wang, M. K. Stewart, Z. Zhao, G. Dominguez, M. H. Thiemens, *Nano Lett.* **2011**, *11*, 4701.